Journal of Solid State Chemistry 184 (2011) 2948–2960

Contents lists available at SciVerse ScienceDirect

Journal of Solid State Chemistry

journal homepage: www.elsevier.com/locate/jssc

Thermal and electronic charge transport in bulk nanostructured $Zr_{0.25}Hf_{0.75}NiSn$ composites with full-Heusler inclusions

Julien P.A. Makongo [a], Dinesh K. Misra [a], James R. Salvador [b], Nathan J. Takas [a], Guoyu Wang [c], Michael R. Shabetai [a], Aditya Pant [a], Pravin Paudel [a], Ctirad Uher [c], Kevin L. Stokes [a,d], Pierre F.P. Poudeu [a,e,f,*]

[a] The Advanced Materials Research Institute, University of New Orleans, New Orleans, LA 70148, USA
[b] Chemical Sciences and Materials Systems Laboratory, General Motors R&D Center, Warren, MI 48090, USA
[c] Department of Physics, University of Michigan, Ann Arbor, MI 48109, USA
[d] Department of Physics, University of New Orleans, New Orleans, LA 70148, USA
[e] Department of Chemistry, University of New Orleans, New Orleans, LA 70148, USA
[f] Laboratory for Emerging Energy and Electronic Materials, Materials Science and Engineering Department, University of Michigan, Ann Arbor, MI 48109, USA

ARTICLE INFO

Article history:
Received 3 June 2011
Received in revised form
19 August 2011
Accepted 26 August 2011
Available online 8 September 2011

Keywords:
Nanocomposite
Half-Heusler
Full-Heusler
Microstructure
Spinodal decomposition
Thermoelectric properties

ABSTRACT

Bulk $Zr_{0.25}Hf_{075}NiSn$ half-Heusler (HH) nanocomposites containing various mole fractions of full-Heusler (FH) inclusions were prepared by solid state reaction of pre-synthesized HH alloy with elemental Ni at 1073 K. The microstructures of spark plasma sintered specimens of the HH/FH nanocomposites were investigated using transmission electron microscopy and their thermoelectric properties were measured from 300 K to 775 K. The formation of coherent FH inclusions into the HH matrix arises from solid-state Ni diffusion into vacant sites of the HH structure. HH(1–y)/FH(y) composites with mole fraction of FH inclusions below the percolation threshold, $y\sim0.2$, show increased electrical conductivity, reduced Seebeck coefficient and increased total thermal conductivity arising from gradual increase in the carrier concentration for composites. A drastic reduction ($\sim$55%) in κ_l was observed for the composite with $y=0.6$ and is attributed to enhanced phonon scattering due to mass fluctuations between FH and HH, and high density of HH/FH interfaces.

1. Introduction

The importance of nanostructures (nanoscale powder or nanostructured bulk composites) in enhancing the figure of merit of a promising thermoelectric material has been widely demonstrated over the past decades through extensive theoretical and experimental studies [1–23]. The success of this approach in improving the figure of merit of thermoelectric (TE) materials has been attributed to: (1) the ability to significantly suppress the lattice thermal conductivity using high densities of matrix/nanoinclusion interfaces or grain boundaries to increase phonon scattering and (2) the enhancement of the Seebeck coefficient due to filtering of low energy carriers at the matrix/inclusion interfaces [24,25]. The efficiency of a TE material is related to the dimensionless figure of merit $ZT=[(S^2\sigma)/\kappa]T$, where S is the Seebeck coefficient, σ is the electrical conductivity, κ is the total thermal conductivity and is the sum ($\kappa=\kappa_e+\kappa_l$) of the electronic contribution (κ_e) and the lattice contribution (κ_l).

In a bulk nanocomposite, one or more nanometer scale inclusion phases are introduced into the matrix of a promising TE material. The electronic, thermal transport and mechanical properties of the resulting nanocomposite markedly differ from those of either of the pristine compounds forming the composite. These properties depend on several parameters such as: (i) the coherency of matrix/nanoinclusion interfaces which is beneficial to carrier mobility through the interfaces, while acoustic phonons are scattered [1–6,26–28]; (ii) the nature and complexity of solid state phase transformations such as spinodal decomposition [4,17], nucleation and growth [1,3,5], or matrix encapsulation [28,29] governing the interaction between the nanoinclusions in the bulk matrix; (iii) the volume fraction of the inclusion phases; (iv) the size, shape, and distribution of the nanoinclusions within the matrix; and (v) the charge transfer at the semiconductor/semimetal/-metal interfaces, which is strongly energy-dependent [19,29]. Seminal works on nanocomposite TE materials have focused on bulk semiconducting matrices containing semiconducting or semimetallic nanoinclusions. These efforts led to significant improvement of the thermoelectric properties mainly due to a large reduction in the lattice thermal conductivity arising from enhanced phonon scattering at interfaces [1,3,5,30].

However, recent theoretical work based on the thermoelectric properties of a bulk semiconducting matrix containing metallic

* Corresponding author at: Laboratory for Emerging Energy and Electronic Materials, Materials Science and Engineering Department, University of Michigan, Ann Arbor, MI 48109, USA. Fax: +1 734 763 4788.
E-mail address: ppoudeup@umich.edu (P.F.P. Poudeu).

0022-4596/$ - see front matter © 2011 Elsevier Inc. All rights reserved.
doi:10.1016/j.jssc.2011.08.036

nanoinclusions has predicted a simultaneous increase in the power factor and a reduction in the thermal conductivity [19]. The improvement in the power factor is mainly due to an increase in the Seebeck coefficient which, in turn, is ascribed to an energy filtering effect [8,19,29]. In the semiconducting matrix, metallic inclusions induce band bending which creates a potential barrier. Such a barrier acts as an energy filter from which low-energy electrons are strongly scattered, while high-energy electrons remain almost unaffected. This filtering effect increases the mean energy per carrier resulting in enhanced Seebeck coefficient. The reduction in the thermal conductivity is thus ascribed to suppression of both electronic and phonon contributions to the thermal conductivity. Starting with already proven and established TE matrices, the most challenging question concerns the ability to synthesize such bulk nanocomposite structures.

In this paper, we report on an elegant and efficient strategy to chemically synthesize bulk half-Heusler (HH) composites containing metallic full-Heusler (FH) inclusions and discuss the effect of the metallic inclusion phases on the thermal and electronic transport properties. HH alloys have been extensively investigated and are classified as a promising thermoelectric material for high temperature power generation. They are narrow band gap semiconductors ($E_g \sim 0.1$–0.4 eV) with large Seebeck coefficients and a relatively high electrical conductivities [32–35]. However, their thermal conductivities are still too high to achieve a ZT above unity. HH alloys crystallize in the cubic MgAgAs-type structure with a unit cell consisting of four interpenetrating *fcc* sublattices, three of which are filled while the fourth remains vacant (Fig. 1a). To fabricate bulk semiconducting HH composites containing metallic FH inclusions, we took advantage of the ability to partially fill vacant sites in the HH structure with elemental Ni (Fig. 1b) to induce precipitates of FH. Precipitates of the FH, coherently embedded into the bulk HH matrix are expected to form due to the insolubility of HH and FH phases (they cannot form solid solutions) as well as the similarity in their unit cell parameters (for a given composition). Here, we investigate the effect of various mole fractions of the FH metallic nanoinclusion phases on the conducting behavior of the semiconducting bulk HH matrix. To this aim, we have chosen the HH alloy, $Zr_{0.25}Hf_{0.75}NiSn$, as the starting matrix given its simple composition and reduced thermal conductivity [36,37]. The bulk-HH/FH composites investigated in this work were prepared by precipitating various mole fractions of FH nanoinclusions in a bulk HH matrix through a solid-state reaction (diffusion process) of polycrystalline powder of a pre-synthesized HH matrix with various concentrations of elemental Ni.

We show that creating local structural disorder by insertion of FH inclusions into a highly crystalline HH bulk matrix results in the modification of its conducting behavior. The electrical conductivity of the composites increases with rising concentration of FH inclusion and its temperature dependence changes from a semiconducting to a semimetallic to a metallic behavior. The maximum power factor was observed at a relatively low mole fraction of FH nanoinclusions ($\sim$12 at% Ni). In addition, we find that high mole fractions of FH nanoinclusions (HH+0.6Ni) result in composites with microstructures consisting of regions of spinodal decomposition between HH and FH coexisting with FH precipitates coherently embedded inside the HH matrix. The spinodal decomposition regions observed here are alternating layers of small domains of HH and FH structures with lattice coherency and with spatial compositional modulation of about 2 nm. This induces a strong reduction ($\sim$55%) in the lattice thermal conductivity due to the high density of matrix/inclusion interfaces. The observed reduction of the lattice thermal conductivity of HH alloys via nucleation and growth and spinodal decomposition mechanisms is a major departure from the traditional strategy based on mass fluctuation through solid solution alloying [38], making the HH matrix with FH inclusions a promising system in the search for advanced high performance thermoelectric materials for high temperature applications.

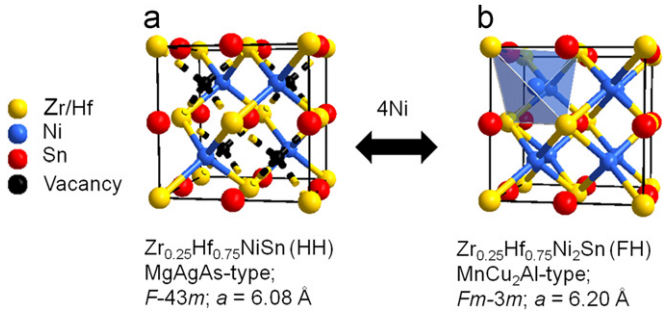

Fig. 1. Relationship between the crystal structures of half-Heusler and full-Heusler alloys. (a) $Zr_{0.25}Hf_{0.75}NiSn$ (HH): MgAgAs-type; $F\bar{4}$; a=6.10 Å [31] and (b) $Zr_{0.25}Hf_{0.75}Ni_2Sn$ (FH): $MnCu_2Al$-type; $Fm\bar{3}$ a=6.24 Å [31].

2. Experimental details

2.1. Synthesis and densification

Polycrystalline $Zr_{0.25}Hf_{0.75}NiSn$ (HH) alloy was obtained as a single phase by solid state reaction of high purity elements. All four components, weighed in the desired stoichiometric ratios (total mass=40.0 g) were thoroughly mixed using an agate mortar and pestle under inert atmosphere. The mixture was loaded into a silica tube which was sealed under a residual pressure of $\sim 1 \times 10^{-3}$ Torr, and heated in a tube furnace at 673 K for 1 day, at 1173 K for 2 weeks, and subsequently slowly cooled to room temperature. The resulting polycrystalline powders (HH) were ball milled (using a planetary ball mill) for 6 h to further reduce the grain size and activate their surfaces. To fabricate the composites, six samples containing 3 g of the pre-synthesized pure $Zr_{0.25}Hf_{0.75}NiSn$ product and various mass fractions (varying from 1 to 10 weight percent) of elemental Ni were prepared under inert atmosphere, sealed under vacuum in fused silica tubes, and then heated for 2 days at 1073 K. Prior to the heat treatment, the mixtures (HH powder and elemental Ni) were ball milled for 20 min to improve the homogeneity. The resulting polycrystalline powders of the HH/FH composites were again ball milled for 20 min to reduce the average particle size and increase the homogeneity of the polycrystalline powders before consolidation into high density pellets.

The densification of the synthesized HH matrix as well as the HH/FH composites was accomplished by spark plasma sintering (SPS). The powders were first cold pressed under a uniaxial pressure of 50 MPa using a graphite die. The temperature was raised to 973 K at a rate of 100 K/min and finally to 1123 K at a rate of 50 K/min. The total pressing time was 12 min including heating ramps. After consolidation was complete, as indicated by no net displacement of the pressing piston, the sample was allowed to cool to room temperature with the pressure released. The overall relative densities of the SPS pressed pellets were measured to be above 95%, reflecting highly packed grains.

2.2. Powder X-ray diffraction

The synthesized bulk HH matrix and the resulting HH/FH composites were structurally characterized by powder X-ray diffraction using monochromated Cu $K\alpha$ radiation (λ=1.54056 Å)

on a PANalytical X'pert Pro powder diffractometer operating at 40 kV and 40 mA.

2.3. DSC analysis

The phase purity of the HH matrix and thermal stability of the synthesized composite materials in the temperature range from 300 to 1173 K were investigated using a differential scanning calorimeter DSC 404F1 *Pegasus* from Netzsch. Measurements were performed on two heating and cooling cycles using approximately 15 mg of finely ground powder samples of the HH bulk matrix or the HH/FH composites.

2.4. Density measurement

The density of loose powders of the HH matrix and the synthesized HH/FH composites were measured at ambient temperature using helium gas pycnometry on a Micromeritics Accupyc II 1340. The relative compaction of the pellets was obtained by dividing the geometrical density (obtained from sample mass and dimensions) with the measured powder density.

2.5. Electron microscopy

The microstructures of SPS specimens of the HH matrix and the HH/FH composites were investigated using a transmission electron microscope (TEM; JEOL-2010) operating at 200 kV. TEM specimens were prepared from the pellets by cutting 3 mm discs using an ultrasonic disc cutter (Fischione 170). The specimens were mechanically polished with a load of 12 g using a dimple grinder (Gatan 1656) and electron-transparent specimens for TEM analysis were achieved by Ar^{+}-ion milling (Fischione 1010). The ion milling was carried out in two steps using a cold stage with a constant temperature of 160 K. The specimens were first milled to perforation over 2 h at 3.5 kV and 5 mA with a 10° milling angle followed by further milling for 30 min at 1 kV and 5 mA with a milling angle of 8°. The elemental analysis was performed using energy dispersive spectroscopy (EDS) attached on the TEM. The goal of the TEM investigation was to characterize the internal structure of the HH matrix as well as that of the HH/FH composites and identify the finest details which could enable better explanation of the observed thermal and electronic transport properties of the materials.

2.6. Electrical properties

The electrical conductivity and Seebeck coefficient were measured simultaneously using a DC four-probe method and a differential voltage/temperature technique, respectively, on a ZEM-3 system from ULVAC-RIKO. The measurements were performed on rectangular bar specimens of approximately 10 mm × 3 mm × 2.5 mm, cut from the SPS consolidated disc-shaped pellets. A low-pressure of helium atmosphere was maintained in the sample chamber during the entire measurement run from 300 K to 775 K. The precision of measurement on the ZEM-3 system is within ±5%.

2.7. Thermal conductivity

The thermal conductivity was calculated from thermal diffusivity and specific heat data measured under flowing N_2 gas (>30 mL/min) using a laser flash apparatus LFA-457 from Netzsch. Measurements were done on disc-shaped pellets ($\phi \approx 12.7$ mm; thickness ≈2–3 mm) fabricated by spark plasma sintering and a Pyroceram 9606 reference material was measured alongside each specimen. Diffusivity data were recorded on heating and on cooling from 300 K to 775 K at increments of 25 K. The thermal conductivity (κ) was calculated using the equation $\kappa = d \times C_p \times D$, where d is the geometrical density of the pellet, C_p is the specific heat (extracted from the laser flash data) and D is the thermal diffusivity. The lattice thermal conductivity (κ_l) was obtained by subtracting the electronic thermal conductivity (κ_e) from the total thermal conductivity (κ). κ_e was estimated using the Wiedemann–Franz law, $\kappa_e = L\sigma T$, where $L = 2.45 \times 10^{-8}\ W\Omega\ K^{-2}$ is the Lorenz factor. The precision of measurement on the Netzsch LFA-457 laser flash apparatus is within ±2%.

2.8. Hall coefficients

Hall coefficients were measured up to 775 K in the magnetic field of ±1 T using a large Oxford air-bore superconducting magnet cryostat that accommodates a small tubular oven and a Hall insert. Measurements are performed on rectangular samples of typically $1 \times 3 \times 9\ mm^3$ in size cut adjacent to the samples on which the electrical resistivity and Seebeck coefficient are measured and pressure contacts are used. The holder with the sample is protected by a quartz tube that is evacuated and backfilled with argon gas. The Hall signal is monitored with a Linear Research AC Bridge (LR-700) operated at a frequency of 17 Hz.

3. Results and discussion

3.1. Synthesis, X-ray diffraction and electron microscopy

The powder X-ray diffraction (PXRD) patterns of the synthesized $Zr_{0.25}Hf_{0.75}NiSn$ (HH) matrix and the HH/FH composites (HH+x wt% Ni) are shown in Fig. 2. All peaks of the HH matrix pattern (Fig. 2a) were indexed to the cubic MgAgAs-type structure with the unit cell parameter $a = 6.09(5)$ Å. No additional peaks from un-reacted elements or from binary intermetallic phases could be detected above the background of the diffraction pattern, indicating the ability to synthesize polycrystalline powders of $Zr_{0.25}Hf_{0.75}NiSn$ (HH) as a single or near single phase in a one step solid state reaction of the elements at temperatures below 1273 K. Despite the high melting temperatures of the elements

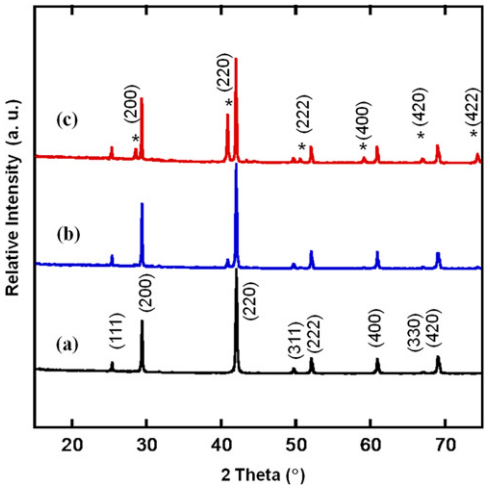

Fig. 2. Selected PXRD patterns of the synthesized composites compared to that of the half-Heusler matrix. (a) $Zr_{0.25}Hf_{0.75}NiSn$ (HH) matrix with $a = 6.09(5)$ Å; (b) HH+2 wt% Ni; (c) HH+5 wt% Ni. * indicates peaks from the full-Heusler ((Hf/Zr)Ni_2Sn) phase with $a = 6.248(2)$ Å. The patterns of the composites obtained with 1, 3 and 10 wt% Ni content are not shown for the clarity of the figure. The (1 1 1), (3 1 1) and (3 3 0) peaks of the FH could not be detected above the background of the diffraction patterns because of their low intensity.

involved, we find that maintaining the reaction mixture around 673 K for 1 day is sufficient to allow molten Sn to diffuse into the remaining solid matrix (Hf, Zr, Ni). At this stage no elemental Sn is present in the mixture and raising the temperature of the furnace to 1173 K helps to accelerate atomic diffusion throughout the solid matrix and achieve a single phase.

This strategy is energy efficient and prevents segregation between elements at high temperatures. These are significant advantages over the traditional ultra-high temperature arc-melting technique, which requires a large amount of energy in addition to the losses of Sn by evaporation which must be accounted for and compensated. We find that successful formation of $Zr_{0.25}Hf_{0.75}NiSn$ by solid state combination of the elements requires a homogeneous mixture of finely divided powders of the starting elements. Additionally, surface activation of fine particles of the starting mixture, which can be achieved by prolonged grinding using a mortar and pestle, is key to facilitating the diffusion processes and the formation of the single phase $Zr_{0.25}Hf_{0.75}NiSn$ in a one-step reaction.

The transmission electron microscopy (TEM) images of a spark plasma sintered pellet of the $Zr_{0.25}Hf_{0.75}NiSn$ is shown in Fig. 3a and b. Bright field TEM images (Fig. 3a) revealed that the pellet is made of large and small densely packed grains of the HH phase. A high magnification image (Fig. 3b) of one of the grains showed excellent crystallinity of the HH matrix. Although the exact stoichiometry of the HH matrix could not be determined, the quaternary composition of the HH grains was verified by elemental analysis (Fig. 3c) and the selected area electron diffraction (SAED) confirmed the face-centered cubic structure of the HH matrix (Fig. 3d).

The next step after the synthesis of a well crystallized, semiconducting HH matrix was to insert nanoinclusions with the full-Heusler structure into the matrix. The diffraction patterns of the synthesized composites (Figs. 2b and c) mainly consist of peaks from the HH matrix together with additional peaks associated with the FH ($(Zr/Hf)Ni_2Sn$) phase resulting from the reaction of the HH matrix with additional elemental Ni. All $h\,k\,l$ diffraction peaks of the FH are shifted to lower 2θ, relative to the HH phase, and were indexed with the cubic $MnCu_2Al$-type structure. The refined unit cell parameter, $a=6.248(2)$ Å is $\sim$2.5% larger than that of the HH matrix, which is consistent with the insertion of additional Ni atoms within the vacant site of the HH structure. No noticeable shift was observed in the peak positions of the HH matrix when comparing powder X-ray patterns of the pristine HH matrix with those of the composites. This suggests that no solid solution is formed between the HH and FH phases during the reaction. In addition, no evidence of elemental Ni could be found in the PXRD patterns of various composites, indicating a complete reaction of the additional elemental Ni with the $Zr_{0.25}Hf_{0.75}NiSn$ matrix to form FH precipitates according to the Eq. (1).

$$Zr_{0.25}Hf_{0.75}NiSn + yNi \rightarrow (1-y)Zr_{0.25}Hf_{0.75}NiSn\ (\text{matrix}) + yZr_{0.25}Hf_{0.75}Ni_2Sn\ (\text{second phase}) \quad (1)$$

The suggested equation is supported by the fact that the intensities of $h\,k\,l$ peaks from the FH phase in the synthesized composites increase with rising Ni content in the starting mixture ($Zr_{0.25}Hf_{0.75}NiSn + x$ wt% Ni). Assuming a full reaction of elemental Ni with the half-Heusler matrix, the synthesized materials in subsequent paragraphs will be referred to as HH(1–y)/FH(y) composites,

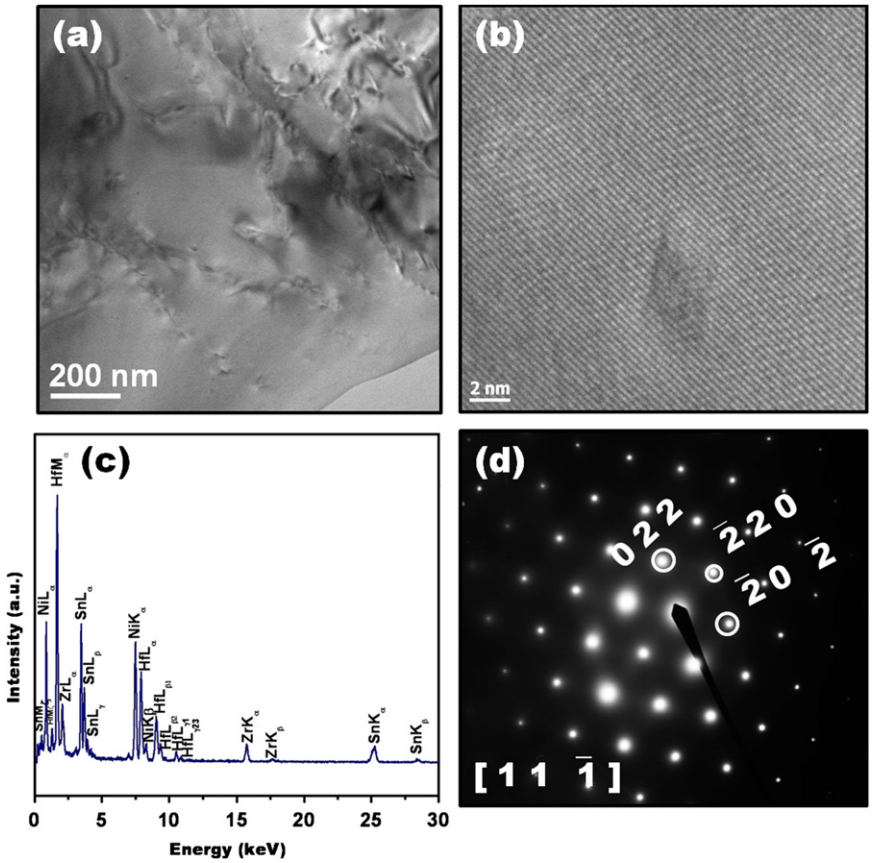

Fig. 3. Transmission electron microscopy study of the HH matrix. (a) Bright field TEM image exhibiting large and small densely packed grains of HH; (b) high magnification of one of the grains, showing excellent crystallinity of the HH phase; (c) energy dispersive spectroscopy (EDS) spectra recorded from the HH matrix showing the presence of all four elements; and (d) selected area electron diffraction (SAED) of one of the grains showing the cubic structure of the HH phase. The SAED micrograph was indexed with the [1 1 $\bar{1}$] zone axis direction of the half-Heusler structure with the lattice parameter $a \approx 6.10$ Å.

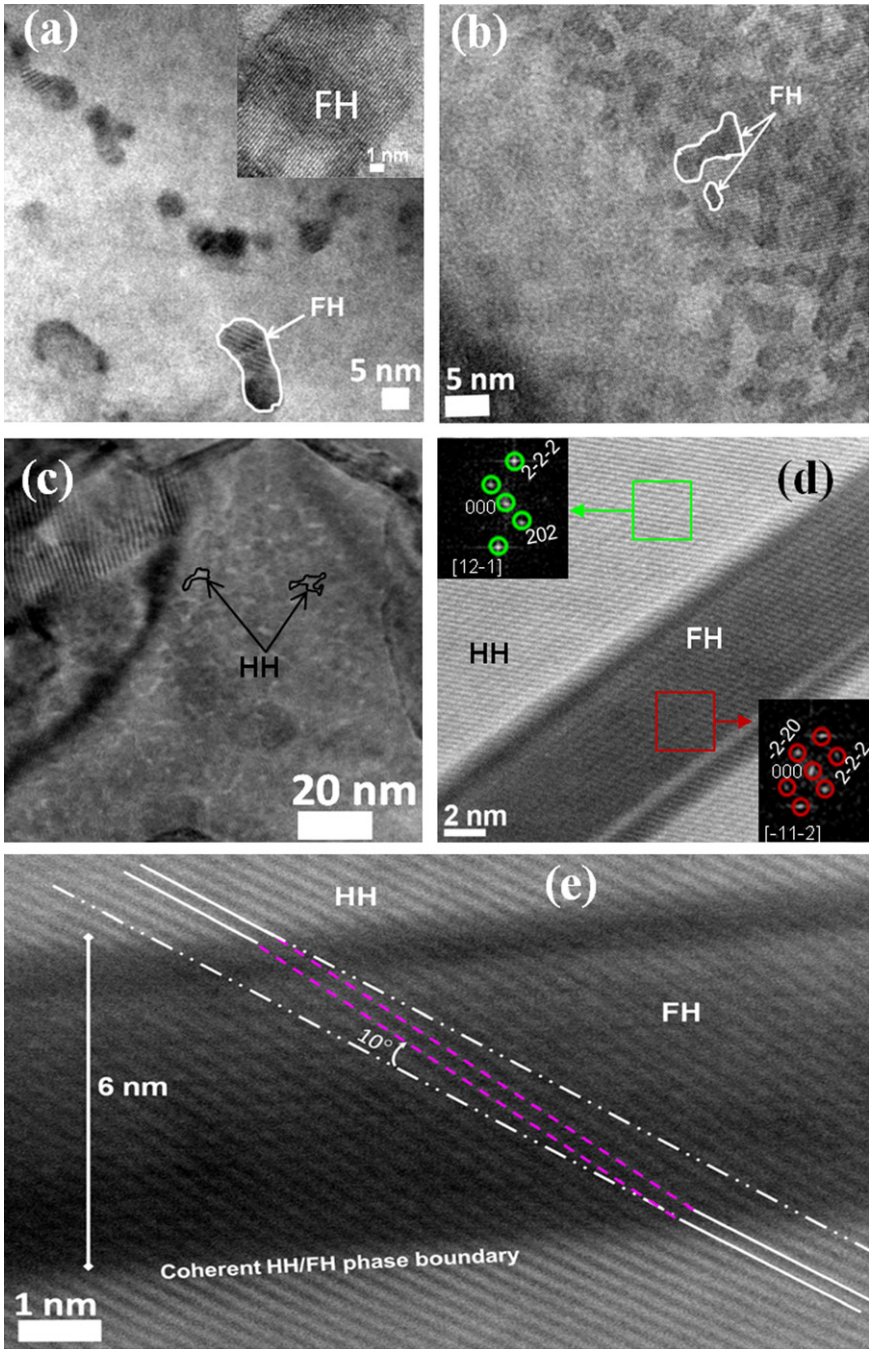

Fig. 4. TEM images of selected HH(1–y)/FH(y) composites. (a) HH(0.91)/FH(0.09) composite from reaction between the pre-synthesized $Zr_{0.25}Hf_{0.75}NiSn$ matrix and 9 at% excess Ni; (b) HH(0.7)/FH(0.3) composite showing interconnections between FH precipitates; (c) HH(0.4)/FH(0.6) composite showing light-gray precipitates with HH structure embedded into a matrix with FH structure; (d) high magnification TEM images of HH(0.7)/FH(0.3) composite showing alternating layers of the matrix and the precipitate. Fast Fourier Transformed (FFT) diffractograms of both regions indicate that the light-gray region corresponds to HH structure with unit cell parameter a=6.10 Å (upper left inset in d) whilst the dark-gray region has a FH structure with a=6.24 Å (lower right inset in d). (e) Details of the tilted coherent phase boundary at the HH/FH interfaces arising from the small difference (2.5–3%) in their cell parameters.

where y=0.06; 0.09; 0.12; 0.30; 0.6 is the mole fraction of full-Heusler (FH).

Fig. 4 shows the microstructure of SPS pressed pellets of selected bulk HH(1–y)/FH(y) composites. Spherical dark-gray precipitates with sizes ranging between 5 and 10 nm can be observed on the TEM micrograph of the composite HH(0.91)/FH(0.09) obtained by reacting the pre-synthesized $Zr_{0.25}Hf_{0.75}$NiSn matrix with 9 at% excess Ni (Fig. 4a). Several of the small precipitates occasionally agglomerate to form larger particles with sizes up to 20 nm. They are highly crystalline and form coherent or semi-coherent boundaries with the matrix (inset of Fig. 4a). Upon increasing the concentration of excess Ni to y=0.3 (HH(0.7)/FH(0.3)), a density of the spherical dark gray precipitates is observed on the TEM images of the resulting composite (Fig. 4b). The precipitates also severely agglomerate to form large particles which in turn form interconnected networks. Further increases in the amount of excess Ni to y=0.6 (HH(0.4)/FH(0.6)) results in the formation of several small light-gray precipitates within a dark-gray matrix (Fig. 4c). This reversal in the contrast of the matrix from light-gray to dark-gray strongly indicates gradual conversion of the existing HH structure of the matrix to FH structure upon increasing the concentration of excess Ni atoms

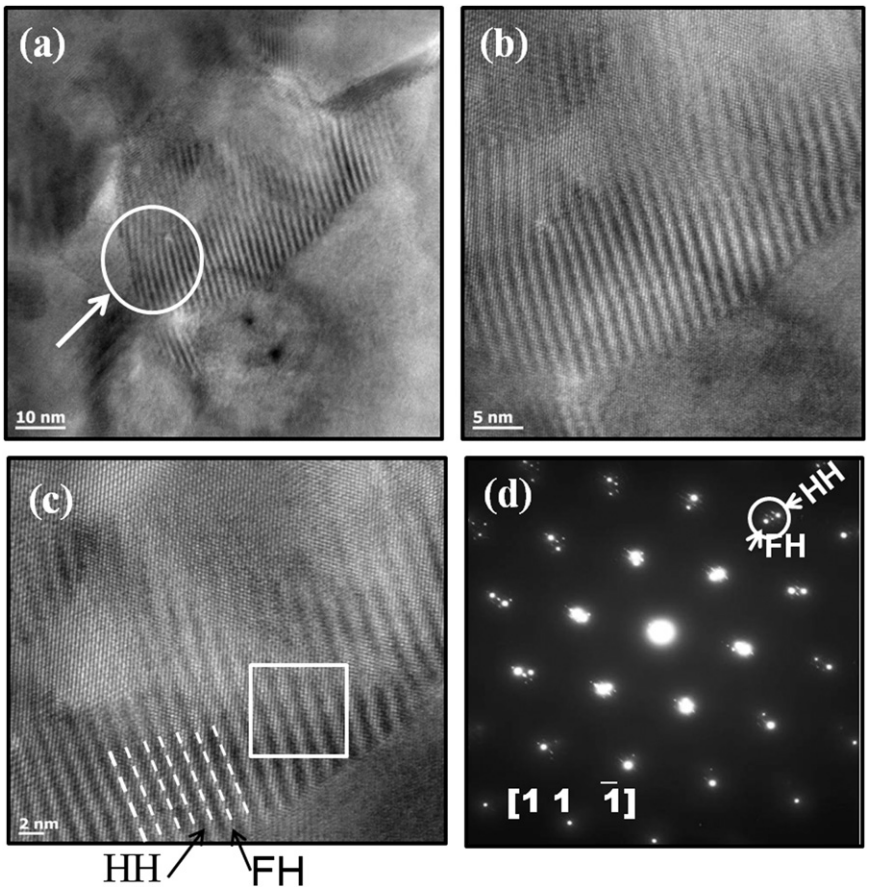

Fig. 5. HRTEM images at various magnifications of the HH(0.4)/FH(0.6) composite. (a) Images revealing the coexistence (arrow and white circle) of HH precipitates together with spinodal decomposition region in the [1 1 $\bar{1}$] zone axis. The spinodal decomposition region is magnified in (b) and (c) to show fine structures of the HH and FH phases alternating along [1 1 $\bar{1}$]. (d) Selected area electron diffraction (SAED) taken from the two phase region (white square in (c)) revealed the coexistence of two structures with very similar unit cell parameters as indicated by the double spots (white circle).

in the starting mixture and is consistent with the suggested chemical Eq. (1). It should be stressed that the dispersion of the dark precipitates within the HH matrix strongly depends on the initial homogeneous or inhomogeneous distribution of elemental Ni within the polycrystalline powder of the HH matrix.

Fig. 4d represents a high magnification TEM image taken from another location of the HH(0.7)/FH(0.3) specimen, showing the interface between alternating layers of the light-gray matrix and the dark-gray precipitates. The width and length of the precipitates are approximately 6 nm and 50 nm, respectively. Fast Fourier transformed (FFT) diffractograms taken from the light-gray region and the dark gray region reveal that the precipitates are oriented along [$\bar{1}$ 1 $\bar{2}$] zone axis (lower right inset in Fig. 4d) whilst the HH matrix is oriented along [1 2 $\bar{1}$] (upper left inset in Fig. 4d). The unit cell parameters calculated from the FFT diffractograms are a=6.24 Å and a=6.10 Å for the dark gray region and light-gray regions, respectively. This clearly indicates that the precipitates crystallize with the FH structure, while the light-gray region corresponds to the matrix with HH structure. The formation of alternating HH and FH layers results in a tilted coherent phase boundary at the interfaces (Fig. 4e) due to the small difference (2.5–3%) in their cell parameters. The tilt angle between atomic planes at the HH/FH phase boundary is approximately $\theta=10^{\circ}$ (Fig. 4e). Although the exact composition of the FH inclusion could not be determined, the similarity between the unit cell parameter (a=6.24 Å) calculated from the FFT diffractogram of the dark-gray region (Fig. 4d) and that of the FH phase (a=6.248(2) Å) refined from the XRD (Fig. 2) suggests a nominal chemical composition of the precipitates close to $Hf_{0.75}Zr_{0.25}Ni_2Sn$ assuming a complete reaction between the pre-synthesized $Zr_{0.25}Hf_{0.75}NiSn$ matrix and the excess elemental Ni. We can therefore conclude based on powder X-ray diffraction and TEM data discussed so far, that both $Zr_{0.25}Hf_{0.75}NiSn$ (HH) and $Zr_{0.25}Hf_{0.75}Ni_2Sn$ (FH) coexist in the composite as matrix and inclusion respectively with high level of lattice coherency. The mole fraction of the FH inclusions within the HH matrix can be controlled by adjusting the amount of additional elemental Ni used according to Eq. (1).

Fig. 5 shows characteristic TEM images of the HH(0.4)/FH(0.6) composite. The white circle and the arrow in Fig. 5a illustrate a region where HH and FH phases form parallel stripes of periodic compositional fluctuations with repeating wavelength, λ=2 nm as highlighted in Fig. 5b and c in the [1 1 $\bar{1}$] zone axis (Fig. 5d). The parallel stripes likely arise from the alternation of HH (light-gray) and FH (dark-gray) formed during the Ni diffusion inside the pre-synthesized HH matrix as described in Fig. 6. This type of phase transformation inducing the snake-like pattern observed in Fig. 5b and c with spatial modulation of the local composition is indicative of spinodal decomposition, which frequently occurs in an unstable region of a phase diagram (temperature-composition) exhibiting a miscibility gap. However, as discussed below in detail, such ordered superlattices of alternating FH and HH units can also be obtained through intergrowth between both sub-structures given their three dimensional similarity.

It should be noted that the existence of a miscibility gap between HH and FH in the system $AB_{2-x}X$ ($0 \le x \le 1$), where A is a transition metal (Ti or V group elements), B is also a transition metal (Fe, Co, or Ni group elements), and X is a main group element (Ga, Sn, or Sb) had been predicted by Jeitschko [31]. The unstable region is located

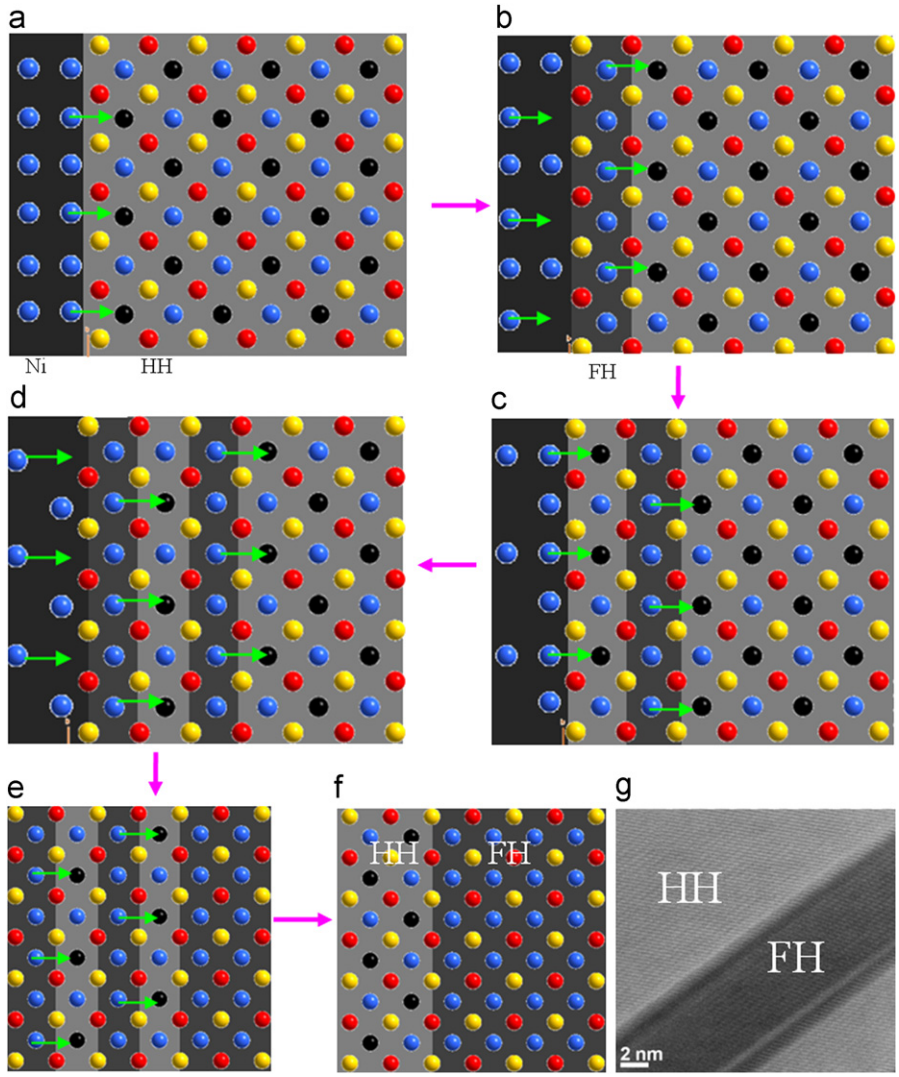

Fig. 6. Proposed Ni diffusion mechanism at the Ni/HH matrix interface and throughout the HH matrix (at the FH/HH interface), leading to the formation of HH/FH composite via solid-state phase transformation. (a) Condition of the Ni/HH interface at the beginning of the diffusion process; (b) formation of the first seed layer of the FH phase, which triggers the diffusion of more Ni towards the Ni/FH interface; (c) simultaneous diffusion at both Ni/HH and FH/HH interfaces; (d) formation of the second FH layer and continuous Ni diffusion at all interfaces (Ni/FH; FH/HH); (e) Ni diffusion at the FH/HH interfaces within the composite (after complete diffusion of elemental Ni atoms into the HH structure) leading to migration and agglomeration of unstable FH seed layers; and (f) formation of stable FH/HH interface away from the initial Ni/HH interface. Blue spheres: Ni; Red spheres: Zr/Hf; Yellow spheres: Sn; Black spheres: Vacant sites within the HH structure. (g) High magnification TEM image of HH(0.7)/FH(0.3) composite illustrating alternating layers of the HH matrix and the FH precipitate. (For interpretation of the references to color in this figure legend, the reader is referred to the web version of this article.)

inside the miscibility gap where the second derivative of the free-energy (G) with respect to composition is negative ($\partial^2 G/\partial c^2 < 0$). In spinodal decomposition, a spontaneous phase separation at the nanoscale occurs in homogeneous supersaturated solutions (solid or liquid), which results in the formation of two phases of different compositions but with identical crystal structure. The spinodal decomposition phenomenon has been extensively studied in the past three decades both theoretically and experimentally in several intermetallic systems [4,15,17,39–46], polymers [47–49], and glassy mixtures [50–52]. The close similarity of the unit cell parameters and crystal structures of the HH ((Zr,Hf)NiSn) and FH ((Zr,Hf)Ni_2Sn) compositions investigated in this work are favorable for the formation, at appropriate local concentrations of both phases (HH and FH), of spinodal decomposition regions through thermally induced Ni diffusion. Selected area electron diffraction (SAED) of the spinodal decomposition domain (white square in Fig. 5c) revealed the coexistence of two structures with quite similar unit cell parameters as illustrated by the doubling of reflections on the SAED micrograph (Fig. 5d). The length and the width of the spinodal decomposition region displayed in Fig. 5a are 100 nm and 35 nm, respectively. The observed spinodal decomposition region on the TEM images of the HH(0.4)/FH(0.6) composite might be explained by the fact that the local concentration gradient of HH and FH in some regions satisfies the minimum free-energy condition.

3.2. Formation of HH(1–y)/FH(y) composites

Although the coexistence of HH and FH phases has been observed previously in the $TiNi_{1.5}Sn$ alloy [53], the composite was obtained after complete melting of the elements using the arc-melting technique and resulted in large, micron-sized FH regions. It is interesting to note that the synthetic method used in this work to achieve the observed nanostructures does not follow the classical extended heat treatment sequence for nucleation and growth and spinodal decomposition type systems, which involves: (i) the homogenization stage where the alloy is heated to a temperature above the miscibility gap in order to form a monophasic structure; (ii) the quenching stage during which the rapid cooling results in the formation of supersaturated solid solution at room temperature, and (iii) the aging stage during which the supersaturated monophase

alloy is heated to a temperature within the range of nucleation and growth or spinodal decomposition followed by annealing for the time required for the decomposition process. The ability to achieve nanometer-scale FH inclusions through pure solid-state diffusion of elemental Ni into the HH structure at 1073 K is therefore the most striking and surprising finding in this study. The formation of alternating HH and FH layers in the synthesized composites as revealed by TEM analysis (Fig. 4d) strongly suggests the following general Ni diffusion mechanism (Fig. 6) leading to the observed solid state phase transformation. The nucleation of the first FH seeds at the Ni/HH interface is facilitated by the three dimensional structural similarity between the FH inclusion and HH matrix (both crystallize with face-centered cubic structures with a small lattice mismatch of ~2.5%, and the distances between Zr/Hf, Sn and Ni atoms are comparable in both structures). The HH phase in this solid state transformation reaction serves the double role of reactant and substrate on which seeds of the FH phase can anchor. The three dimensional structural similarity of the FH and HH phases is also favorable for endotaxial growth of the FH inclusions leading to the formation of the observed coherent interfaces with the HH matrix. In addition, the condition of the interface between grains of elemental Ni and grains of the HH matrix (Ni/HH) such as: (1) the large Ni concentration gradient (Fig. 6a), (2) the availability of a large number of vacant sites into which Ni atoms can move, and more importantly (3) the availability of Ni atoms with sufficient thermal energy to overcome the energy barrier for diffusion (activation energy) given the temperature of the reaction (1073 K), are favorable for the initiation of the Ni diffusion process. Once the first FH layer is formed at the interface (Fig. 6b), more Ni atoms diffuse towards the Ni/FH interface simultaneously with Ni diffusion at the newly formed FH/HH interface. This diffusion of Ni from the FH sub lattice to the HH structure creates vacant sites and a new Ni/HH interface (Fig. 6c). The Ni diffusion at the Ni/HH interface will continue to convert the HH subunits into the FH structure as long as there are Ni atoms available. The formation of each FH layer increases the number of Ni diffusion fronts within the HH matrix (Fig. 6d). After the Ni at the interface is depleted, further diffusion at the FH/HH interfaces is driven by the relative stability of the FH domain (Fig. 6e) and the availability of adjacent vacant sites in the HH structure. The ability of FH seed layers to migrate throughout the HH matrix via Ni diffusion at the FH/HH interfaces could lead to (1) the formation of regions with large concentrations of FH within the HH matrix reminiscent of features obtained from the nucleation and growth mechanism or to (2) the formation of alternating layers of FH and HH with spatial compositional modulation wavelength (λ) varying from 2 nm to 3 nm (3–5 unit cells of HH and FH), similar to features resulting from a spinodal decomposition mechanism (Fig. 6f). In recent years, nucleation and growth as well as the spinodal decomposition mechanism have been treated as important strategies to design inhomogeneous composite materials (containing finely dispersed microstructures) with significantly enhanced physical and mechanical properties. The most interesting and fundamental question arising from this work is how do the observed microstructures affect the electronic and thermal transport within the synthesized HH(1–y)/FH(y) composites.

3.3. Electronic charge transport

Fig. 7a shows the temperature dependence of the electrical conductivity of HH(1–y)/FH(y) (y=0.06, 0.09, 0.12, 0.30, 0.60)

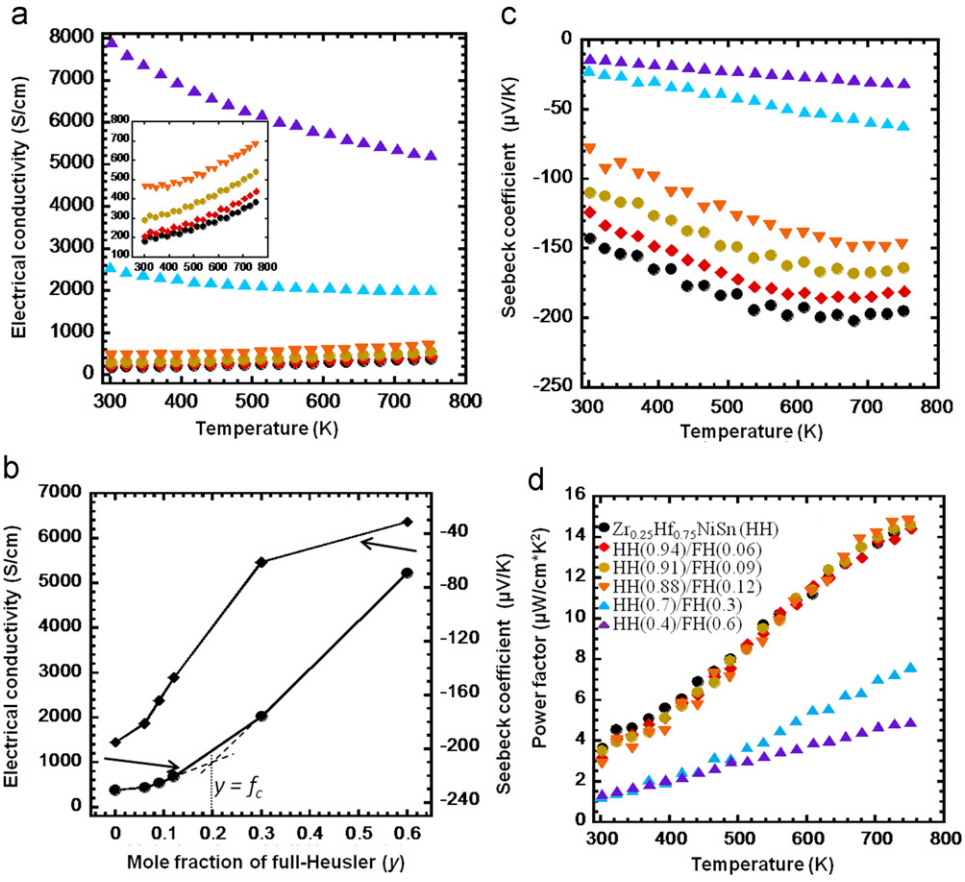

Fig. 7. Electronic transport properties of HH(1–y)/FH(y) composites. (a) Temperature dependent electrical conductivity and (b) variation of the electrical conductivity and thermopower at 750 K with increasing mole fraction of the FH inclusions; an electrical-percolation network is expected to form for y=0.2. (c) Temperature dependent Seebeck coefficient and (d) temperature dependence of the power factor. The precision of measurement on our ZEM-3 system is within ± 5%.

composites. Three general trends can be observed depending on the mole fraction of the FH in the composite. For HH/FH composites with low FH content ($y \leq 0.12$), the electrical conductivity increases monotonically with temperature suggesting that the semiconducting character ($\partial\sigma/\partial T > 0$) of the synthesized HH(1–y)/FH(y) composites is retained up to 12 mol% of the FH inclusion. Regardless of the temperature, the electrical conductivity of composites ($y \leq 0.12$) gradually increases with the mole fraction of the FH inclusion (Fig. 7a). At 750 K, the electrical conductivities of the composites range from 300 S/cm for $y=0$ to 650 S/cm for $y=0.12$ (Fig. 7b). The observed increase in the electrical conductivity of the composites with increasing FH content is opposite to the trend reported by Hohl et al. [54] in ZrNiSn/Ni composites prepared by arc-melting and annealing. The decrease in the electrical conductivity was attributed to an increased scattering of charge carriers due to the large number of structural defects arising from the sample fabrication using arc-melting. In this work, the solid-state reaction technique used to synthesize the HH matrix as well as the composites allows sufficient time for the formation of well crystallized HH and FH phases and the similarity in their crystal structure and lattice parameters favors the formation of coherent HH/FH interfaces which minimizes scattering of charge carriers in the composites. Increasing the mole fraction of the FH inclusion to 30% resulted in a large increase in the electrical conductivity in the measured temperature range. This abrupt change in the electrical conductivity of the HH(1–y)/FH(y) composites upon increasing the mole fraction of FH inclusion from $y=0.12$ to 0.3, suggests that the percolation threshold, $y=f_c$, above which metallic FH inclusions start building conducting network within the HH matrix has been exceeded (Fig. 7b). At compositions near the percolation threshold, $f_c \sim 0.2$, the metallic FH inclusions are not necessary geometrically interconnected (Fig. 4b); however, the electrical-percolation network responsible for the drastic increase in the electrical conductivity is formed via electrons tunneling between two adjacent FH inclusions [55]. The electrical conductivity of the HH(0.7)/FH(0.3) composite shows a very weak temperature dependence ($\partial\sigma/\partial T \sim 0$) suggesting a semimetal-like-character (Fig. 7a). At 300 K, the electrical conductivity of the composite is $\sim$2500 S/cm and decreases to $\sim$2000 S/cm at 750 K. Further increasing the mole fraction of the FH inclusions to 60% yielded a composite with metallic-like conductivity ($\partial\sigma/\partial T < 0$). As shown in Fig. 4c, the HH(0.4)/FH(0.6) composite can be viewed a metallic FH matrix with semiconducting HH inclusions. The electrical conductivity monotonically decreases with rising temperature from $\sim$8000 S/cm at 300 K to $\sim$5500 S/cm at 750 K.

Fig. 7c shows the temperature dependence of the thermopower of HH(1–y)/FH(y) composites. All samples showed negative values of the thermopower indicating n-type conducting behavior in the measured temperature range. The thermopowers of the composites increase with temperature regardless of the mole fraction of the FH inclusions. However, the strength of the dependence of the thermopower on the temperature decreases with increasing mole fraction of the FH phase in the composite. Samples with FH content below the percolation threshold ($y < 0.2$) showed strong increase in the thermopower with temperature. For example, the thermopower values for the sample with 6 mol% FH inclusions increase from -125 μV/K at 300 K to -180 μV/K at 650 K and remain constant thereafter with a further increase in temperature. Weak dependence of the thermopower on temperature was observed for the samples with FH content above the percolation threshold ($y=0.3$ and 0.6). Regardless of the temperature, the thermopower of the composites decreases with increasing mole fraction of the FH inclusions. This trend is consistent with the observed increase in the electrical conductivity with increasing concentration of the metallic FH inclusion. The drop in the thermopower is gradual for composites with low FH content ($y < 0.2$) while a more dramatic loss in the thermopower is observed for the HH(0.7)/FH(0.3) and HH(0.4)/FH(0.6) composite in which the metallic FH inclusions are interconnected into networks. At 750 K, the thermopower values rapidly decrease from -200 μV/K for $y=0$ to -30 μV/K for $y=0.6$ (Fig. 7b).

The temperature dependence of the power factor of HH(1–y)/FH(y) composites is shown in Fig. 7d. The power factors of the composites with low FH content increase rapidly with increasing temperature while samples with a high mole fraction of FH showed weaker increases of the power factor with temperature. Regardless of the temperature, the synthesized HH(1–y)/FH(y) composites showed only marginal changes in the power factor for low mole fractions of the FH inclusions ($y < 0.2$) suggesting that the observed decrease in the thermopower is compensated by the increase in the electrical conductivity. The highest power factor of $\sim$15 μW/cm K^2 was obtained at 750 K for the composition with 12 mol% FH inclusions. Increasing the FH content to 30 mol% and 60 mol% resulted in a drastic decrease in the power factor due to the observed large decrease in the thermopower arising from the contribution of the networks of metallic inclusions to the electronic transport.

To better understand the observed changes in the electronic transport properties of the synthesized HH(1–y)/FH(y) composites with the mole fraction of the FH inclusions, we have carried out Hall effect measurements from 300 K to 775 K and have examined the variation of charge carrier concentration (n) and mobility (μ) with both the temperature and the mole fraction of the FH inclusions (y). Fig. 8a shows the temperature dependence of the Hall coefficient (R_H) of the synthesized composites. Except for the composite containing 60% FH which shows very small positive values of the Hall coefficient, the R_H of the synthesized HH(1–y)/FH(y) composites remains negative throughout the entire temperature range suggesting that electrons are the majority charge carriers. The absolute values of the Hall coefficient, $|R_H|$, drastically decrease with increasing mole fraction of the FH inclusions. R_H values at room temperature decrease from -11.3×10^{-2} cm^3/C for the HH matrix ($y=0$) to -4×10^{-4} cm^3/C for the composite with 30% FH inclusion (Table 1). The sharp decrease in the Hall coefficient with increasing FH content suggests that the filling of vacant sites in the HH structure with additional Ni atoms gradually drives the semiconducting HH matrix to metallic behavior presumably due to an increase in the mole fraction of metallic FH inclusions within the HH matrix. The Hall coefficients of the HH matrix as well as that of the composites with 6 mol%, 9 mol% and 12 mol% FH inclusions increase with rising temperature, whereas composites containing 30% and 60% FH inclusions show a slight decrease in R_H with increasing temperature (Fig. 8a). Overall, the strength of the variation of R_H with temperature notably decreases with increasing FH content in the composite.

Carrier concentrations in the synthesized materials were calculated from the Hall Effect data using the equation $n = 1/(e \times |R_H|)$, where R_H is the Hall coefficient and e is the electron charge. This equation assumes a transport dominated by a single carrier. Regardless of the temperature, the carrier concentration in the synthesized composites increases with increasing FH content (Fig. 8b). This explains the observed decrease in the thermopower of the composites as the mole fraction of FH inclusions increases. The room temperature values of charge carrier concentrations in HH(1–y)/FH(y) composites are summarized in Table 1. The carrier concentrations in the HH matrix as well as in composites containing up to 12% FH inclusions fall between 10^{19} and 10^{21} cm^{-3}, which is within the range of expected carrier concentrations in doped semiconductors [35,56] and is consistent with the observed temperature dependence of the electrical conductivity of this group of samples

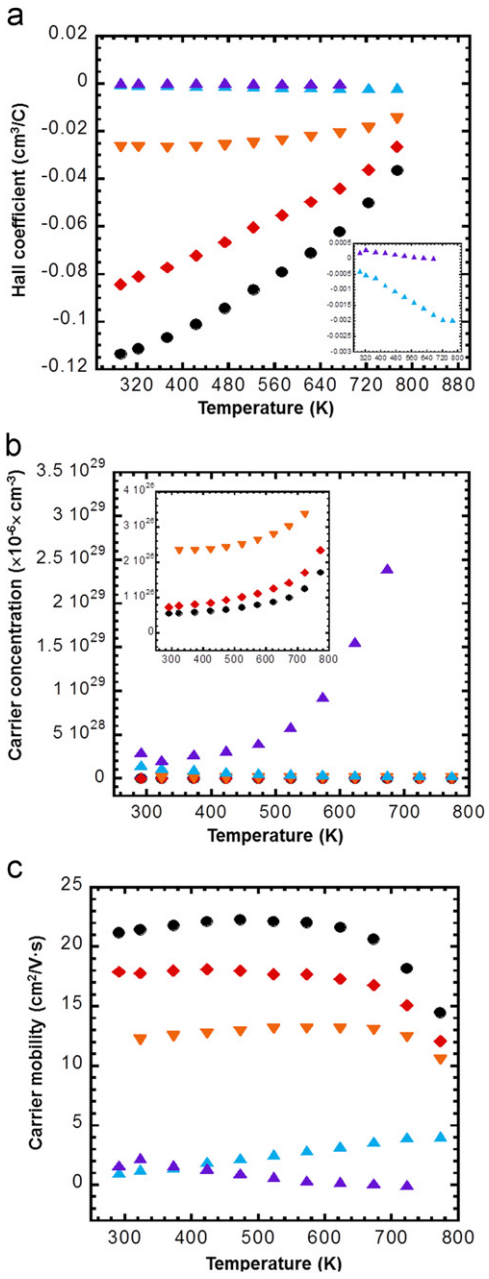

Fig. 8. Temperature dependence of charge transport parameters of HH(1–y)/FH(y) composites. (a) Hall coefficient; (b) carrier concentration; and (c) carrier mobility. The precision on measurement of Hall coefficient is within $\pm 5\%$.

Table 1
Room temperature Hall coefficient (R_H), carrier concentrations ($n=1/e|R_H|$), carrier mobility ($\mu_H=\sigma|R_H|$), Seebeck coefficient (S), electrical conductivity (σ) and the total thermal conductivity (κ) of HH(1–y)/FH(y) composites.

y	R_H ($\times 10^{-2}$ cm^3/C)	n (cm^{-3})	μ_H (cm^2/V s)	S (μV/K)	σ (S/cm)	κ (W/mK)
0	−11.4	5.5×10^{19}	21.2	−143	178	5.37
0.06	−8.4	7.4×10^{19}	17.9	−124	207	5.47
0.09	–	–	–	−110	288	5.55
0.12	−2.7	2.3×10^{20}	12.2	−79	464	6.18
0.30	-4.1×10^{-2}	1.5×10^{22}	1.1	−22	2566	6.91
0.60	2.1×10^{-2}	3.0×10^{22}	1.6	−14	7907	8.90

($y<0.2$). The observed gradual increase in the carrier concentration in composites with $y<0.2$ suggests that at these concentrations the FH inclusions behave more like dopants for the semiconducting HH matrix. Increasing the FH content to $y=0.3$ and 0.6 results in a drastic increase in the carrier concentrations up to $\sim10^{22}$ cm^{-3}. At these high mole fractions of the FH phase (both $y=0.3$ and 0.6), the inclusions agglomerate into large particles which further link together to form metallic networks within the HH matrix (Fig. 4b and c). In this situation, the observed electronic transport properties of the composite must be viewed as the sum of contributions from both the semiconducting HH and metallic FH components. Therefore, the large values of the carrier concentration in composites with $y=0.3$ and 0.6 are consistent with their semimetallic or metallic behavior and also explain the observed large increase in the electrical conductivity of the composites (Fig. 7a).

Interestingly, the carrier concentration in the synthesized composites changes with temperature. This is especially so for composites containing low FH content ($y<0.2$) that show a rapid increase of the carrier concentration at temperatures above 500 K (inset of Fig. 8b). This again is consistent with their more semiconducting behavior and also explains the observed saturation of the thermopower at high temperatures. When the mole fraction of the FH inclusions in the composite is increased to 30 mol%, the resulting material behaves like a heavily doped semiconductor with an almost constant carrier concentration over the measured temperature range. The most interesting observation is perhaps the sudden sharp increase in the carrier concentration above 500 K in the composite containing 60 mol% of the FH phase. This is the sample that actually displays a small positive Hall coefficient. The electronic transport in this sample is clearly dominated by the metallic FH phase which represents 60% of the composite although the sudden large increase in the carrier concentration above 500 K also suggests significant contributions from the semiconducting HH phase. This interplay between the semiconducting HH network and the metallic FH network prevents drastic drops in the electrical conductivity with rising temperature, which explains the observed high electrical conductivity (5500 S/cm) and low Seebeck coefficient (-30 μV/K) at 750 K for this composite ($y=0.6$).

The carrier mobility (μ_H) in the synthesized HH(1–y)/FH(y) composites was estimated using the equation $\mu_H=\sigma|R_H|$, where σ is the electrical conductivity and R_H is the Hall coefficient. The room temperature values of the carrier mobility for all samples are listed in Table 1. The mobility of the synthesized HH(1–y)/FH(y) composites strongly decreases with increasing mole fraction of the FH inclusions. At 300 K, the carrier mobility decreases from ~20 cm^2/Vs for the FH-free sample to ~2 cm^2/Vs for the composites with the highest concentrations of the FH phase ($y=0.3$ and 0.6). For composites with low content of FH inclusions, the magnitude of the carrier concentration is in the order of 10^{20} cm^{-3} and the carrier mobility ranges from 18 to 12 cm^2/Vs in the temperature range from 300 to 750 K. These values are consistent with the carrier concentration and mobility reported for the heavily doped n-type half-Heusler alloy [57]. The carrier mobility in the HH matrix is ~20 cm^2/Vs at 300 K and remains almost constant up to 600 K (Fig. 8c). Further increase of the temperature results in a rapid decrease of the mobility, probably due to the observed increase in the carrier concentration which also increases carrier–carrier scattering. A similar trend was observed in the temperature dependence of the carrier mobility in all HH(1–y)/FH(y) composites with low FH content ($y<0.2$). The composite with 30 and 60 mol% FH inclusions showed drastically low carrier mobility presumably due to increased contributions from the network of metallic FH inclusions. For the composite with $y=0.3$, a slight increase of the mobility with increasing temperature is observed, whereas the carrier mobility in the composite with 60 mol% FH inclusions decreases with increasing temperature. These findings suggest that the electronic transport in the synthesized composites strongly depends on the

mole fraction of the metallic FH inclusions as well as their interactions with the HH matrix.

3.4. Thermal conductivity and figure of merit

The temperature dependence of the total and lattice thermal conductivity of the synthesized HH(1–y)/FH(y) composites is shown in Fig. 9. The total thermal conductivity (κ) of the HH matrix at 300 K is ~5.4 W/mK. As the temperature increases, κ slightly decreases to a minimum value of 4.3 W/mK around 700 K and increases thereafter with further increase in temperature. The observed minimum in the total thermal conductivity of the HH matrix results from the combination of the increased electronic thermal conductivity, κ_e (due to increased electrical conductivity) and decreased lattice thermal conductivity, κ_l (due to enhanced phonon scattering). A similar trend was observed in the temperature dependence of the κ of all HH/FH composites with low FH content ($y < 0.2$). HH/FH composites containing high mole fractions of the FH phase ($y = 0.3$ and 0.6) showed a marginal increase in κ with temperature. This trend results from the large increase in the electrical conductivity of the composites with 30 mol% and 60 mol% FH inclusions. Regardless of the temperature, κ of the synthesized HH/FH composites increases with increasing fraction of the FH phase.

This result is consistent with the observed increase in the electrical conductivity arising from increased carrier concentrations. The lattice thermal conductivity of the synthesized HH/FH composites decreases with increasing temperature. Regardless of the temperature, κ_l remains almost constant for composites with up to 9 mol% FH inclusions. This suggests the formation of coherent, phonon-transparent interfaces between the HH matrix and the FH inclusions. The formation of such interfaces is probably favored by the fact that the FH inclusion phases are derived from the existing HH structure and the Ni diffusion process presumably does not induce the formation of high densities of dislocations at the interfaces for low concentrations of FH inclusions. A marginal increase in κ_l was observed for composites with 12 and 30 mol% FH inclusions. The increase in κ_l of the composites (rather than the expected reduction due to phonon scattering at the interfaces) is probably due to the formation of networks between metallic FH inclusions (Fig. 6f) leading to a FH substructure with κ_l higher than that of the HH matrix. Interestingly, increasing the FH content in the composite to 60 mol% resulted in a drastic reduction of κ_l of the composite. At room temperature, κ_l decreased from 5.4 W/m K for the HH ($Zr_{0.25}Hf_{0.75}NiSn$) matrix to 2.6 W/mK for the composite with 60 mol% FH. In addition, κ_l decreases with increasing temperature and reaches a record low value of 1.4 W/mK at 775 K for a half-Heusler based thermoelectric material. Lower values of κ_l can be expected at even higher temperatures. We attribute this strong reduction in κ_l of the bulk HH(0.4)/FH(0.6) composite to the formation of nano-domains consisting of alternating layers of FH and HH phases with a spatial modulation of ~2 nm (Fig. 5c). These features are reminiscent of the spinodal decomposition regions observed in $Pb_{1-x}Sn_xTe$–PbS [4] and $Ge_x(Sn_yPb_{1-y})_{1-x}Te$ [17] composites, which are believed to be responsible for the strong reduction in the lattice thermal conductivity in these materials. The formation of such nanostructures with coherent atomic planes between HH and FH domains in the HH(0.4)/FH(0.6) composite facilitates electron flow while phonons are strongly scattered due to the increased density of the HH/FH interfaces. Although alternating layers of HH and FH phases was also observed in the HH(0.7)/FH(0.3) composite (Fig. 4d), the large thickness of the FH layers (in the order of 6 nm) and the resulting low density of HH/FH interfaces does not allow for strong phonon scattering and large reduction in κ_l.

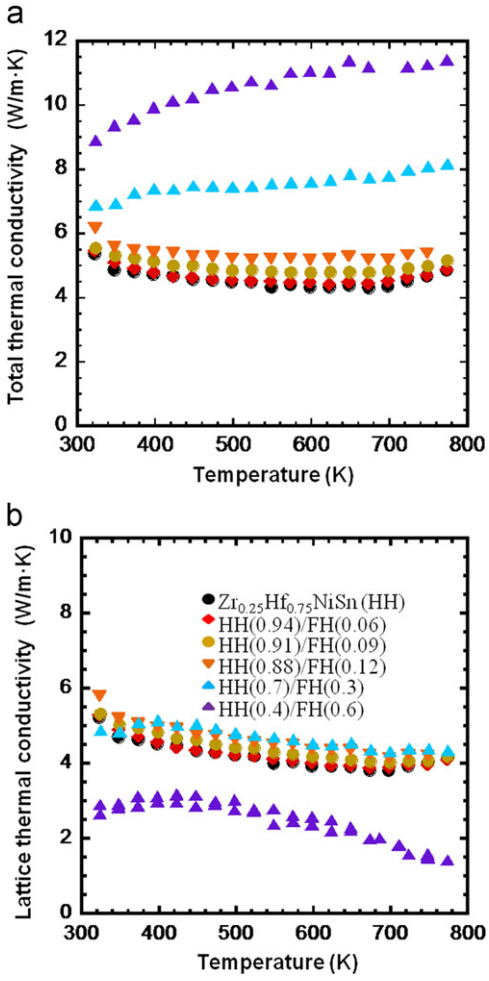

Fig. 9. Temperature dependent thermal conductivity of HH(1–y)/FH(y) composites. (a) Total thermal conductivity and (b) lattice thermal conductivity. The precision of measurement our Netzsch LFA-457 laser flash apparatus is within ±2%.

The temperature dependence of the thermoelectric figures of merit (ZT) of the synthesized HH(1–y)/FH(y) composites is shown in Fig. 10. The figure of merit of the matrix is $ZT \sim 0.02$ at 300 K. This value remains almost constant for composites containing up 12 mol% of FH inclusions. The ZT of samples with low FH content ($y < 0.2$) rapidly increase with temperature. However, the strength of the temperature dependence of ZT decreases with increasing mole fraction of the FH inclusions. At 750 K, the figures of merit of the synthesized HH(1–y)/FH(y) composites sharply decrease with increasing mole fractions of the FH phase. The highest figure of merit, $ZT \sim 0.23$, was observed at 750 K for the HH matrix. The reduction in the figures of merit of the synthesized HH(1–y)/FH(y) composites results from large decreases in the Seebeck coefficient and increases in κ_e arising from increased carrier concentration upon increasing the mole fraction of the metallic FH inclusions.

4. Conclusions

We have demonstrated the ability to chemically create bulk nanostructured $Zr_{0.25}Hf_{0.75}NiSn$ half-Heusler (HH) composites with metallic $Zr_{0.25}Hf_{0.75}Ni_2Sn$ full-Heusler (FH) nanometer-scale inclusions formed *in situ* via solid state reaction of pre-synthesized bulk HH matrix with elemental Ni. The mole fraction of the FH inclusions in the composite can be controlled by adjusting the HH/Ni mole ratio. The formation of the FH inclusions arises from the solid state diffusion of elemental Ni atoms into vacant sites in the HH structure. Transmission electron microscopy studies

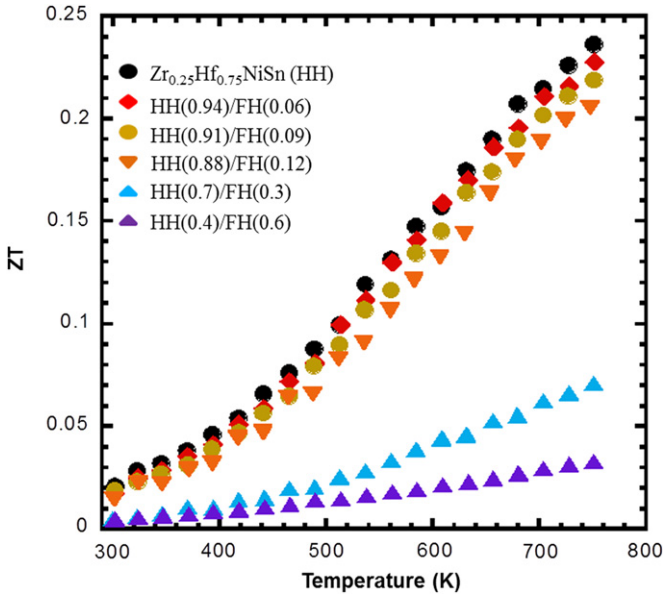

Fig. 10. Temperature dependence of the figure of merit of HH(1–y)/FH(y) composites.

revealed that the FH inclusions in the synthesized composites are in the order of 5–20 nm and become interconnected to form metallic networks for FH mole fractions above the percolation threshold, $y=0.2$. The micrograph of the composite containing 60 mol% of the FH phase showed several regions consisting of alternating layers of HH and FH phases with a spatial modulation of about 2 nm (Fig. 5c) reminiscent of spinodal decomposition. The investigation of the electronic transport of the synthesized HH/FH composites showed a strong electronic interaction between the HH matrix and the FH inclusions, which induces a drastic change in the conduction behavior of the composites from semiconducting ($y \leq 0.12$) to semimetallic ($y=0.3$) to metallic ($y=0.6$) as the mole fraction of the FH inclusions increases. This resulted in a large increase in σ and a decrease in S of the composites, due to increased charge carrier concentration with increasing mole fraction of the FH inclusions. The κ of the composites also increases with increasing mole fraction of the FH inclusions due to a large increase in κ_e. However, κ_l of the composites with low FH content ($y < 0.2$) remains comparable to that of the HH matrix. A strong reduction ($\sim$55%) of κ_l was observed for the composite containing 60 mol% of the FH phase. This drastic reduction in κ_l is attributed to the enhanced phonon scattering at multiple HH/FH interfaces in the spinodal decomposition regions. No improvement in the overall ZT of the synthesized composites was observed, due mostly to a simultaneous decrease of S and an increase in κ arising from the increased charge carrier concentration. However, the ability to create coherently embedded metallic FH inclusions within the semiconducting HH matrix holds great promise for the design of HH/FH composites with high ZT. The increased carrier concentration and the resulting decrease in power factor in the composites arise from the large size (5–20 nm) of the FH inclusions and the formation of networks between them. We anticipate that by reducing the size of the FH inclusions (2–3 nm) and breaking the interconnections between them, it will be possible to fabricate new composite materials with enhanced S (through filtering of low energy electrons at the HH/FH interfaces due to quantum confinement) and drastically reduced κ_l (via strong phonon scattering at multiple HH/FH interfaces) leading to enhanced figures of merit. The exploration of this strategy is underway.

Acknowledgments

The authors gratefully acknowledge financial support from DARPA (contracts # HR0011–08-1-0084 and W91CRB-10-C-0189). This work made use of the laser flash diffusivity apparatus (Netzsch-LFA457) purchased with funds from the Louisiana Board of Regents (Grant # LEQSF(2008-09)–ENH-TR-58). The work at the University of Michigan is supported by the Center for Solar and Thermal Energy Conversion, an Energy Frontier Research Center funded by the U.S. Department of Energy, Office of Basic Energy Sciences under Award No. DE-SC0000957.

References

[1] P.F.P. Poudeu, J. D'Angelo, A.D. Downey, J.L. Short, T.P. Hogan, M.G. Kanatzidis, Angew. Chem. Int. Ed. 45 (2006) 3835.
[2] P.F.P. Poudeu, J. D'Angelo, H.J. Kong, A. Downey, J.L. Short, R. Pcionek, T.P. Hogan, C. Uher, M.G. Kanatzidis, J. Am. Chem. Soc. 128 (2006) 14347.
[3] P.F.P. Poudeu, A. Gueguen, C.I. Wu, T. Hogan, M.G. Kanatzidis, Chem. Mater. 22 (2010) 1046.
[4] J. Androulakis, C.H. Lin, H.J. Kong, C. Uher, C.I. Wu, T. Hogan, B.A. Cook, T. Caillat, K.M. Paraskevopoulos, M.G. Kanatzidis, J. Am. Chem. Soc. 129 (2007) 9780.
[5] J. Androulakis, K.F. Hsu, R. Pcionek, H. Kong, C. Uher, J.J. DAngelo, A. Downey, T. Hogan, M.G. Kanatzidis, Adv. Mater. 18 (2006) 1170.
[6] E. Quarez, K.F. Hsu, R. Pcionek, N. Frangis, E.K. Polychroniadis, M.G. Kanatzidis, J. Am. Chem. Soc. 127 (2005) 9177.
[7] L.D. Chen, X.Y. Huang, M. Zhou, X. Shi, W.B. Zhang, J. Appl. Phys. 99 (2006) 064305/1.
[8] M.S. Dresselhaus, G. Chen, M.Y. Tang, R.G. Yang, H. Lee, D.Z. Wang, Z.F. Ren, J.P. Fleurial, P. Gogna, Adv. Mater. 19 (2007) 1043.
[9] Ø. Prytz, A.E. Gunnæs, O.B. Karlsen, T.H. Breivik, E.S. Toberer, G.J. Snyder, J. Taftø, Phil. Mag. Lett. 89 (2009) 362.
[10] H.J. Kim, E.S. Božin, S.M. Haile, G.J. Snyder, S.J.L. Billinge, Phys. Rev. B 75 (2007) 134103.
[11] T. Ikeda, L. Collins, V.A. Ravi, F. Gascoin, S.M. Haile, G.J. Snyder, Chem. Mater. 19 (2007) 763.
[12] T. Ikeda, S.M. Haile, V.A. Ravi, H. Azizgolshani, F. Gascoin, G.J. Snyder, Acta Mater. 55 (2007) 1227.
[13] T. Ikeda, V.A. Ravi, G.J. Snyder, J. Mater. Res. 9 (2008) 2538.
[14] T. Ikeda, E. Toberer, V. Ravi, G. Snyder, S. Aoyagi, E. Nishibori, M. Sakata, Scr. Mater. 60 (2009) 321.
[15] T. Ikeda, V.A. Ravi, G.J. Snyder, Met. Mat. Trans. A 41 (2010) 641.
[16] G. Joshi, H. Lee, Y.C. Lan, X.W. Wang, G.H. Zhu, D.Z. Wang, R.W. Gould, D.C. Cuff, M.Y. Tang, M.S. Dresselhaus, G. Chen, Z.F. Ren, Nano Lett. 8 (2008) 4670.
[17] Y. Gelbstein, B. Dado, O. Ben-Yehuda, Y. Sadia, Z. Dashevsky, M.P. Dariel, Chem. Mater. 22 (2010) 1054.
[18] R. Yang, G. Chen, M.S. Dresselhaus, Phys. Rev. B 72 (2005) 125418.
[19] S.V. Faleev, F. Leonard, Phys. Rev. B 77 (2008) 214304.
[20] L. Salamancayoung, D.L. Partin, J. Heremans, J. Appl. Phys. 63 (1988) 1504.
[21] W. Kim, J. Zide, A. Gossard, D. Klenov, S. Stemmer, A. Shakouri, A. Majumdar, Phys. Rev. Lett. 96 (2006) 045901.
[22] M. Zhou, J.-F. Li, T. Kita, J. Am. Chem. Soc. 130 (2008) 4527.
[23] M.M. Zhou, J.-F. Li, B. Du, D.W. Liu, T. Kita, J. Solid State Chem. 182 (2009) 3138.
[24] J.P. Heremans, C.M. Thrush, D.T. Morelli, Phys. Rev. B 70 (2004) 115334.
[25] X. Yan, G. Joshi, W. Liu, Y. Lan, H. Wang, S. Lee, J.W. Simonson, S.J. Poon, T.M. Tritt, G. Chen, Z.F. Ren, Nano Lett. 11 (2011) 556.
[26] M.G. Kanatzidis, Chem. Mater. 22 (2010) 648.
[27] J.R. Sootsman, J.Q. He, V.P. Dravid, S. Ballikaya, D. Vermeulen, C. Uher, M.G. Kanatzidis, Chem. Mater. 22 (2010) 869.
[28] J.R. Sootsman, R.J. Pcionek, H.J. Kong, C. Uher, M.G. Kanatzidis, Chem. Mater. 18 (2006) 4993.
[29] J.P. Heremans, C.M. Thrush, D.T. Morelli, J. Appl. Phys. 98 (2005) 063703.
[30] K.F. Hsu, S. Loo, F. Guo, W. Chen, J.S. Dyck, C. Uher, T. Hogan, E.K. Polychroniadis, M.G. Kanatzidis, Science 303 (2004) 818.
[31] W. Jeitschko, Metall. Trans. 1 (1970) 3159.
[32] F.G. Aliev, N.B. Brandt, V.V. Moshchalkov, V.V. Kozyrkov, R.V. Skolozdra, A.I. Belogorokhov, Z. Phys. B Condens. Matter 75 (1989) 167.
[33] F.G. Aliev, V.V. Kozyrkov, V.V. Moshchalkov, R.V. Scolozdra, K. Durczewski, Z. Phys. B Condens Matter 80 (1990) 353.
[34] S.J. Poon, in: T.M. Tritt (Ed.), Semiconductor and Semimetals, vol. 70, Academic, New York, 2001, p. 37.
[35] J.W. Simonson, S.J. Poon, J. Phys.: Condens. Matter 20 (2008) 255220.
[36] S.R. Culp, S.J. Poon, N. Hickman, T.M. Tritt, J. Blumm, Appl. Phys. Lett. 88 (2006) 042106.
[37] J.P.A. Makongo, D.K. Misra, J. Salvador, N. Takas, K. Stokes, H. Gabrisch, P.F.P. Poudeu, Mater. Res. Soc. Symp. Proc. 1267 (2010) DD05/11.
[38] Q. Shen, L. Chen, T. Goto, T. Hirai, J. Yang, G.P. Meisner, C. Uher, Appl. Phys. Lett. 79 (2001) 4165.
[39] J.W. Cahn, Acta Met. 9 (1961) 795.

[40] J.W. Cahn, Acta Met. 10 (1962) 179.
[41] J.W. Cahn, Acta Met. 14 (1966) 1685.
[42] J.W. Cahn, TMS AIME 242 (1968) 166.
[43] K.B. Rundman, J.E. Hilliard, Acta Met. 15 (1967) 1025.
[44] E.P. Butler, G. Thomas, Acta Met. 18 (1970) 347.
[45] J.S. Langer, Ann. Phys. (NY) 65 (1971) 53.
[46] J.S. Langer, M. Bar-on, Ann. Phys. (NY) 78 (1973) 421.
[47] Z.Q. Lin, H.D. Zhang, Y.L. Yang, Macromol. Chem. Phys. 200 (1999) 943.
[48] P. Pincus, J. Chem. Phys. 75 (1981) 1996.
[49] P.G. Degennes, J. Chem. Phys. 72 (1980) 4756.
[50] G.F. Nielson, Phys. Chem. Glass 10 (1969) 54.
[51] M. Tomozawa, R.K. MacCrome, H. Herman, J. Am. Ceram. Soc. 53 (1970) 62.
[52] N.S. Andreev, G.G. Boiko, N.A. Bokov, J. Non-Cryst. Solids 5 (1970) 41.
[53] T. Morimura, M. Hasaka, M. Yoshimoto, J. Alloy Compd. 416 (2006) 155.
[54] H. Hohl, A.P. Ramirez, C. Goldmann, G. Ernst, B. Wolfing, E. Bucher, J. Phys.–Condens. Matter 11 (1999) 1697.
[55] C.W. Nan, Y. Shen, J. Ma, Annu. Rev. Mater. Res. 40 (2010) 131.
[56] V. Ponnambalam, P.N. Alboni, J. Edwards, T.M. Tritt, S.R. Culp, S.J. Poon, J. Appl. Phys. 103 (2008) 063716.
[57] C. Uher, J. Yang, S. Hu, D.T. Morelli, G.P. Meisner, Phys. Rev. B 59 (1999) 8615.